Systems Pharmacology Screening Reveals Mertk and other Targetable Kinases in Supratentorial Ependymomas

Marina Chan[1], Songli Zhu[1], Zach Russell[1], Sonali Arora[1], Aleena Arakaki[1], Deby Kumasaka[1], Frank Szulzewsky[1,2,3], Antony Michealraj[4], Eric C Holland[1*], and Taranjit S Gujral[1 *]

[1]Human Biology Division, Fred Hutchinson Cancer Research Center, Seattle, WA, USA

[2]Huntsman Cancer Institute, University of Utah, Salt Lake City, UT 84112, USA

[3]Department of Neurosurgery, Clinical Neurosciences Center, University of Utah, Salt Lake City, UT 84112, USA

[4]Department of Department of Neurological Surgery, University of Pittsburgh School of Medicine, Pittsburgh, PA, USA

*Correspondence: eholland@fredhutch.org, or tgujral@fredhutch.org

ABSTRACT

Ependymomas (EPN) are central nervous system tumors arising from ependymal cells, primarily affecting young children and accounting for 10% of intracranial tumors in children and 4% in adults. Current treatments are limited to surgery and radiotherapy, with chemotherapy providing minimal benefit. Over 70% of supratentorial ependymomas (ST-EPNs) are driven by ZFTA-RELA fusions (ZFTA-RELA^{fus}), which are associated with poor prognosis. Recent molecular classifications have identified two distinct ST-EPN clusters, E1 and E2, with the E1 cluster predominantly composed of ZFTA-RELA^{fus} tumors. However, effective targeted therapies for these tumors remain lacking. Here, we show that the ZFTA-RELA^{fus} mouse model closely mirrors the human E1 cluster, validating its use for therapeutic discovery. Using this model and a systems polypharmacology approach called Kinome Regularization, we identified mer tyrosine kinase (Mertk) as a key regulator of ZFTA-RELA^{fus} cell viability and proliferation. Genetic depletion or pharmacological inhibition of Mertk reduced cell growth *ex vivo* and treatment with the clinical-grade Mertk inhibitor significantly suppressed tumor proliferation *in vivo*. Mechanistically, both human E1 tumors and mouse ZFTA-RELA^{fus} tumors showed elevated Mertk expression, with Mertk inhibition leading to decreased activity of pro-survival pathways. Further, substantial overlap (>80%) between genes upregulated in ZFTA-RELA^{fus} tumors and those downregulated following Mertk inhibition treatment suggest a dependency on Mertk-mediated signaling for tumor growth. These findings highlight Mertk as a promising therapeutic target and support the clinical development of Mertk inhibitors for treating human E1 subtype and ZFTA-RELA^{fus} -driven ependymomas.

INTRODUCTION

Ependymomas, part of the glioma family, constitute 10% of intracranial tumors in children and 4% of brain and spinal cord tumors in adults[1]. Supratentorial (ST), posterior fossa, and spinal ependymomas have been divided into clinically significant and molecularly distinct subgroups[2, 3]. The treatment for all ependymomas remains limited to surgery and radiotherapy. Chemotherapy is rarely used, except in some pediatric cases as an alternative to radiation therapy and is generally ineffective. Next-generation sequencing studies have identified recurrent chromosomal translocations in a subset of ST-EPN, leading to distinct fusion oncogenes[3, 4]. Notably, 72% of ST-EPN cases feature ZFTA-RELA gene fusions (ZFTA-RELA^{fus}), with patients experiencing a 5-year progression-free survival rate of less than 30%. Recently, Arora et al. used bulk RNA-seq analysis of 370 ependymomas, combined with dimensionality reduction, to identify two distinct clusters of ST-EPNs, E1 and E2, each characterized by unique gene fusions, and pathway regulations[5]. The E1 cluster was predominantly composed of ZFTA-RELA^{fus} tumors. Despite advances in understanding the biology of ZFTA-RELA^{fus} ST-EPNs, no therapies specifically targeting the fusion product have been developed. However, identifying specific vulnerabilities downstream of ZFTA-RELA^{fus} may provide new therapeutic opportunities.

Previously, we developed a systems polypharmacology-based method called Kinome Regularization (KiR) to identify kinases that regulate specific phenotypes, such as the growth of EPN cancer cells[6]. KiR leverages the fact that most kinase inhibitors (KIs) are not highly specific but instead affect multiple targets. By exploiting this polypharmacology property in a set of well-characterized kinase inhibitors, we can use machine learning to pinpoint and deconvolute the kinases responsible for a given quantitative trait. A computationally derived set of 32 kinase

inhibitors targets over 90% of the kinome[6, 7]. We have successfully applied this approach in various biological contexts, including identifying kinases that regulate cancer cell migration[6, 8, 9], prostate cancer cell growth[7], SARS-CoV-2-induced cytokine release in monocytes[10], liver-stage malaria[11], herpes virus[12], and cytokine secretion[13], highlighting the versatility of KiR in studying a wide range of phenotypes.

Expression of ZFTA-RELA^{fus} in nestin-expressing cells in mice *in vivo* has been previously shown to be sufficient to form EPN with characteristics similar to human ST-EPN [14], and in this manuscript, we leveraged this mouse model and KiR-based functional screening to identify kinases essential for the growth of ZFTA-RELA^{fus} -driven EPN. Our study demonstrated that the ZFTA-RELA^{fus} -driven mouse model mimicked the E1 expression cluster and identified the pivotal role of mer tyrosine kinase (MERTK) in this cluster, which is uniquely vital for the viability and proliferation of ZFTA-RELA^{fus}-expressing EPN cells. We found that genetic depletion or pharmacological inhibition of Mertk hindered ZFTA-RELA^{fus} EPN cell growth *in vitro* and significantly diminished tumor slice viability. Further, treated with a clinical-grade Mertk inhibitor reduced proliferation in ZFTA-RELA^{fus} EPN tumors in mice. Consistently, we observed significant upregulation of MERTK and its ligand, Gas6, in ZFTA-RELA^{fus} human EPN compared to low-grade ST-EPN or YAP^{FUS} EPN tumors. Mechanistically, the expression of Mertk and Gas6 is dependent on ZFTA-RELA^{fus} EPN. Knockdown of ZFTA-RELA^{fus} or inhibition of Mertk activity led to a decrease in the activity of multiple pro-survival and growth pathways, including MEK/ERK and PI3K/AKT. Thus, we postulate that ZFTA-RELA^{fus} rewires the network to create dependency on Mertk-mediated signaling for EPN growth and progression. Our findings delineate the molecular mechanisms of ZFTA-RELA^{fus}-driven tumor formation and

validate compounds inhibiting ST-EPN tumor growth in preclinical models, with the ultimate aim of advancing candidates for clinical evaluation.

RESULTS

Comparing human ependymoma subtypes with the ZFTA-RELA^{FUS} mouse model. Previous studies, including our own, have demonstrated that the expression of the ZFTA-RELA^{fus} in nestin-expressing brain cells is sufficient to induce EPN in mice[4, 14, 15]. To model this, we utilized the RCAS/tva system for postnatal cell-type-specific gene transfer[15]. Specifically, an RCAS retroviral vector encoding the ZFTA-RELA^{fus} was used to infect nestin-expressing cells in *Nestin-tva* mice. This was achieved through intracranial injection of DF1 chicken fibroblasts, transfected to produce the vector. Tumor development occurred within 70–120 days, and affected mice were identified based on clinical signs (e.g., weight loss, poor grooming) and MRI-confirmed intracranial tumors. Harvested tumors were processed for further analysis, including microtissues, and cell culture (**Fig. 1A**). Differential gene expression analysis between naïve brain tissue and ZFTA-RELA^{fus} tumors revealed 3,401 upregulated and 3,997 downregulated genes (**Fig. 1B**), highlighting the effectiveness of the RCAS/tva system in modeling ZFTA-RELA^{fus} -driven ependymomas and provide a foundation for further investigating the molecular mechanisms underlying tumor development.

To better understand the biology of this mouse model and its relevance to human disease, we compared it to human samples. Recently, Arora et al. analyzed bulk RNA-seq data from 370 ependymomas, 888 medulloblastomas, and 100 fetal brain samples to establish a comprehensive reference landscape for these diseases[5]. Uniform processing, batch correction, and dimensionality reduction revealed four distinct clusters: two representing medulloblastoma and two representing ependymoma (E1 and E2) (**Fig. 1B**). When analyzing the gene fusion profiles of the EPN-E1 and EPN-E2 clusters, Arora et al observed that the EPN-E1 group was predominantly composed of supratentorial ependymomas (ST-EPNs) with the majority of ZFTA-

RELA^{fus} tumors, representing 87% of cases. The E1 and E2 clusters displayed distinct gene fusions, kinase expression profiles, and pathway regulations, with 3,264 genes upregulated and 3,829 downregulated in E1 compared to E2 (**Fig. 1C**). Using volcano plot analysis, we observed that genes upregulated in ZFTA-RELA^{fus} mouse tumors corresponded to those upregulated in the E1 cluster, while genes downregulated in the mouse model were similarly downregulated in E1 (or upregulated in E2). These data suggest that the ZFTA-RELA^{fus} mouse model closely mirrors the E1 subtype of human ependymomas (**Fig. 1D**). Pathway analysis further revealed that the pathways upregulated in the ZFTA-RELA^{fus} mouse model were also enriched in EPN-E1 human samples, but not in EPN-E2 samples, underscoring the biological similarities between the two (**Fig. 1E**), underscoring the RELA-ZFTA fusion's critical role in driving tumor formation and distinguishing the EPN-E1 subtype.

System pharmacology screening applied in ZFTA-RELA^{FUS} EPN. Next, we combined cancer cells derived from mouse ZFTA-RELA^{fus}-expressing EPN tumors (referred as ZR1) with polypharmacology-based screening to identify kinases crucial for the growth of ZFTA-RELA^{fus} EPN cells (**Fig. 2A**). We initiated our study by screening a training set of 37 computationally selected inhibitors, collectively targeting a broad range of kinases, and quantified their effect on the growth of EPN cells expressing ZFTA-RELA^{fus}. Staurosporine, a multi kinase inhibitor was used as a positive control (**Fig. S1, Table S1**). Each kinase inhibitor was tested at eight concentrations, and its effect on cell growth was measured using a real-time growth assay. A total of 73,728 microscopy images were generated, processed, and analyzed for KiR modeling. Changes in the viability of ZR1 cells in response to each training set KI was used as the response variable for elastic net–regularized multiple linear regression. The explanatory variables in this regression were the residual activities of the 298 human kinases in the presence of these selected inhibitors. Model performance was

evaluated using leave-one-out cross-validation (LOOCV) to measure the mean squared error (MSE) between predicted and observed drug responses. In LOOCV, the activity profiles of 36 drugs were used to train the model, which then predicted the remaining drug's effect on ZR1 cell growth. The MSE between predicted and observed changes in cell growth was used to assign an error score to each model. The optimized model achieved over 90% accuracy (**Fig. 2B**). The models with the lowest mean squared errors collectively identified the 12 most "informative kinases" (out of 298) that may regulate the growth of ZFTA-RELA^{fus} cells **(Fig. 2B)**. These include several receptor tyrosine kinases, such as members of the fibroblast growth factor receptor (Ffgr) family, Mertk, c-Kit, Ptk6, and Epha1, highlighting potential targets for developing targeted therapies.

Mertk plays an important role in the growth of ZFTA-RELA^{FUS}- expressing EPN cells.

To validate the accuracy of the KiR predictions, we depleted the levels of 12 KiR-predicted kinases and assessed their effect on ZR1 cell viability. A reduction in the expression of each kinase was confirmed by quantitative PCR, with each kinase showing at least a 50% decrease in expression compared to the non-targeting siRNA control (**Fig. S1**). Our data showed that knockdown of 9 out of 12 kinases led to a statistically significant decrease in cell viability compared to scrambled siRNA-transfected controls (**Fig. 2C**). Notably, knockdown of Mertk resulted in more than a two-fold reduction in cell viability in ZFTA-RELA^{fus} EPN cells. To further confirm the role of these kinases, we monitored the growth of ZR1 cells with depleted levels of Mertk, Fgfr1, Epha1, Epha6, Ptk6, Acvr1, Acvr1b, Pim3, and Irak1 using live cell imaging. Our data indicated that knockdown of Mertk, Epha1/6, Ptk6, Acvr1/b, Pim3, and Irak1 led to a significant decrease in the growth of ZR1 cells compared to either un-transfected or siRNA control transfected ZR1 cells (**Fig. 2D**). While the roles of Fgfr1 and Fgfr3 have been previously implicated in aggressive ependymomas[16, 17], the involvement of Irak1, which regulates NF-kB activity[18] (a known

hallmark of ZFTA-RELA^{fus} EPN), further validates our KiR predictions. However, the role of other kinases, particularly Mertk, has not been previously implicated in EPN, highlighting a novel aspect of our findings.

Next, we assessed whether any of the KiR-predicted and experimentally validated kinases are aberrantly expressed in ZFTA-RELA^{fus} human tumors. We analyzed previously reported transcriptomic changes in EPN tumors with ZFTA-RELA^{fus} compared to low-grade tumors from the same location and YAP fusion-driven EPN tumors[3]. Our analysis revealed that *MERTK*, *ACVR1B*, and *PIM3* are significantly upregulated in ZFTA-RELA^{fus}-driven human tumors (**Fig. 3A**). Interestingly, *FGFR1* expression was elevated in both ZFTA-RELA^{fus} and YAP^{fus} tumors compared to low-grade tumors. Consistently, analysis using dimensionality reduction and clustering of human EPN tumors revealed that MERTK, FGFR1, EPHB4, ACVR1B, and PIM3 were predominantly enriched in the E1 cluster, predominantly consisting of ZFTA-RELA^{fus} tumors. (**Fig. 3B**). These findings support the relevance of the identified kinases as promising therapeutic targets in ZFTA-RELA^{fus} -driven EPN. Of these, we experimentally confirmed that ZFTA-RELA^{fus} EPN mouse tumors showed increased levels of Mertk protein compared with naïve brain (**Fig. 4A**). Together, these findings underscore the potential role of Mertk and other kinases in the proliferation and survival of ZFTA-RELA^{fus} -driven ependymomas.

MERTK is a direct ZFTA-RELA^{FUS} target, and the ZFTA promotor is activated by the ZFTA-RELA fusion via MERTK activity.

Previously, it was shown that in addition to activating the NFκB pathway, ZFTA-RELA^{fus} drives a neoplastic transcriptional program by binding to thousands of unique sites across the genome, activating pathways enriched in MAPK and focal adhesion networks[19, 20]. We investigated whether ZFTA-RELA^{fus}could directly activates MERTK signaling. ChIP-seq analysis from two

recent EPN studies revealed prominent binding sites for ZFTA-RELA^{fus} in the promoter regions of both Mertk and its cognate ligand, Gas6, in mouse EPN cells (**Fig. 4B**). Further, we observed elevated levels of Gas6 in E1 EPN subcluster compared to E2 subcluster (**Fig. 3B**), suggesting that ZFTA-RELA^{fus} could prime the activation of autocrine Gas6-Mertk signaling in cancer cells. To validate this, we knocked down ZFTA-RELA^{fus} in ZR1 cells and assessed changes in *Mertk* expression (**Fig. 4C**). Our data showed that the knockdown of ZFTA-RELA^{fus} led to a significant decrease in the mRNA expression of *Mertk*, *Gas6*, and *Ccnd1* (cyclin D1, a known ZFTA-RELA^{fus} downstream target gene) (**Fig. 4C)**. Furthermore, knockdown of ZFTA-RELA^{fus} resulted in decreased phosphorylation of several pro-growth and survival signaling proteins, including Akt, S6 ribosomal protein, eIF4G, and Mek-Erk (**Fig. 4D)**. These findings suggest that ZFTA-RELA^{fus} not only activates the NFκB pathway but also promotes Mertk signaling by directly binding to its promoter region, highlighting a dual mechanism by which ZFTA-RELA^{fus} drives ependymoma progression.

Previous studies have shown that Mertk regulates intracellular pro-survival and anti-apoptotic signaling pathways in cancer cells and skews macrophage polarization towards a pro-tumor M2-like phenotype in the tumor microenvironment [21-23]. To investigate the contribution of Mertk activation in ZFTA-RELA^{fus} -expressing cancer cells, we stimulated ZR1 cells with Gas6 and observed a robust increase of the phosphorylation of Erk1/2, Akt and S6 ribosomal protein within 5 minutes, indicating that Gas6-Mertk signaling is functional and intact in ZFTA-RELA^{fus} cancer cells (**Fig. 5A**). Given that Gas6 can also activate other members of the TAM receptor family, including Axl and Tyro3, we sought to confirm that the activation of the MAPK and AKT pathways in response to Gas6 is specifically due to Mertk. We treated ZR1 cells with the Mertk inhibitor MRX2843 prior to Gas6 stimulation (**Fig. 5B**). Our data showed that Mertk

inhibition significantly blocked the activation of several downstream pathways, including Mek/Erk and Akt/S6 **(Fig. 5B)**, suggesting that the Mertk receptor is a key driver of Gas6-mediated signaling in ZFTA-RELA^{fus} cells.

MERTK inhibition decreases EPN cell growth *in vitro* and proliferation of ZFTA-RELA^{FUS} EPN tumors in mice.

Having established that Mertk signaling is functional in ZFTA-RELA^{fus} cells and plays a crucial role in activating pro-survival and growth pathways, we next evaluated the efficacy of a clinical-grade Mertk inhibitor, MRX-2843, which can cross the blood-brain barrier[24, 25]. We tested the effectiveness of this inhibitor in 2D cell cultures, 3D tissue slices, and in mice. Our data show that MRX-2843 significantly reduced the growth of ZR1 cells, with an EC_{50} of ~ 200 nM (**Fig. 6A**). Consistently, Mertk inhibition was selectively effective in four different patient-derived ZFTA-RELA^{fus}-expressing cell lines compared to ZFTA-MAML-expressing cells **(Fig. 6B)**. Further, MRX-2843 treatment reduced the viability of mouse ZFTA-RELA^{fus} EPN tumor slices *ex vivo* in a dose-dependent manner (**Fig. 6C**). In mice, a short-term MRX-2843 treatment led to a significant decrease in proliferative cancer cells, as measured by Ki67 staining in HA (ZFTA-RELA^{fus}) positive cells (**Fig. 6D**). Molecular analysis of MRX-2843-treated ZFTA-RELA^{fus} tumors compared to vehicle-treated controls revealed a substantial downregulation of key fusion marker genes and tumor-associated pathways. Specifically, treatment with MRX-2843 led to the complete suppression of the Ccnd1, which is critical for cell cycle progression in EPN[26]. In addition, genes involved in extracellular matrix (ECM) remodeling, such as various collagens, Lumican (Lum), and Integrin β1 (Itgb1), were significantly downregulated, indicating a disruption in tumor structural integrity and invasive potential (**Fig. 6E**). Furthermore, inflammatory signaling genes, particularly Lif, known to contribute to tumor progression and

immune evasion[27], were also markedly reduced following MRX-2843 treatment. Together, these data suggests that Mertk plays an important role in the growth of ZFTA-RELA^{fus} cells and tumors by disrupting multiple essential regulators of ependymoma progression, including extracellular matrix remodeling and immune evasion genes.

To gain a comprehensive understanding of the pathways and processes affected by Mertk inhibition in ZFTA-RELA^{fus} EPN tumors, we conducted unbiased transcriptomic profiling. Short-term treatment (5 days) with MRX-2843 resulted in significant gene expression changes, with 3,868 genes downregulated and 3,514 genes upregulated compared to vehicle-treated tumors (**Fig. 7A**). Notably, there was substantial overlap between genes upregulated in ZFTA-RELA^{fus} tumors and those downregulated following MRX-2843 treatment, indicating that Mertk inhibition directly disrupts tumor-promoting pathways (**Fig. 7B**). Mertk inhibition also decreased *Zfta* expression, a downstream target of the ZFTA-RELA^{fus}, suggesting a feed-forward loop that promotes tumor progression (**Fig. 7C**). Gene Set Enrichment Analysis (GSEA) of significantly downregulated genes following Mertk inhibitor treatment revealed strong enrichment of pathways related to epithelial-mesenchymal transition (EMT), interferon signaling, and inflammatory responses (**Fig. S2**). Consistently, Gene Ontology analysis of the downregulated genes revealed significant enrichment in pathways related to ECM organization, and cytokine signaling, while the upregulated genes were enriched in pathways associated with neuronal systems and GPCR signaling (**Fig.7D**). Finally, PROGENy pathway analysis[28] comparing naïve brain tissue and ZFTA-RELA^{fus} tumors revealed significant enrichment of pro-oncogenic pathways, including WNT, JAK-STAT, and NF-κB signaling (**Fig.7E**). Notably, all these pathways were markedly downregulated in Mertk inhibitor-treated ZFTA-RELA^{fus} tumors. Collectively, these findings highlight the therapeutic potential of targeting MERTK with MRX-

2843 in ZFTA-RELA^{fus}-driven ependymomas, demonstrating a substantial impact on tumor growth, viability, and the suppression of critical oncogenic pathways.

DISCUSSION

Broadly, targeting specific pathways in cancer is challenging due to the presence of multiple concurrent and redundant drivers, especially in primary cancers of the central nervous system, where the blood-brain barrier further limits treatment options. However, some tumors driven by single events essential for tumor survival, such as chromosomal translocations or rearrangements resulting in gene fusions, can be effectively targeted by drugs aimed at these genetic aberrations. For example, the BCR-ABL fusion in chronic myeloid leukemia and the corresponding success of imatinib provide robust and sustained therapeutic targets[29]. Similarly, the ZFTA-RELA^{fus} is a singular event that drives ependymomas and thus could be targeted by agents that directly inhibit the fusion protein. However, directly targeting the ZFTA-RELA^{fus} protein, a constitutively active transcription factor, is challenging. Therefore, targeting proteins downstream of the RELA fusion oncoprotein that are essential for tumor transformation represents an attractive alternative. Kinase inhibitors, with more than 80 kinases clinically approved, represent one of the major classes of anti-cancer drugs[30]. Identifying kinases downstream of the ZFTA-RELA^{fus} could accelerate clinical translation and offer a promising strategy for targeted therapy.

Recently, Arora *et al*.[5] identified two distinct expression-based EPN clusters, E1 and E2, each defined by unique gene fusions, kinase gene expression profiles, and pathway regulations. Notably, the E1 cluster was predominantly composed of ZFTA-RELA^{fus} ST-EPN tumors. Importantly, in this study, comparative analysis revealed that the gene expression patterns in the ZFTA-RELA^{fus} mouse model closely resembled those of the human E1 cluster (**Fig 1**). This strong similarity supports the use of this mouse model as a valuable tool for identifying potential therapeutic targets for the E1 subtype of ST-EPN.

Here, we utilized ZFTA-RELA^{fus} mouse model and applied a systems pharmacology-based approach to identify druggable kinases downstream of ZFTA-RELA^{fus} in ST-EPN, offering promising opportunities for developing effective treatments for these aggressive tumors. We identified several kinases, including Mertk, Epha1/6, Fgfr1, Ptk6, and Acvr1, as critical for the growth and survival of ZFTA-RELA^{fus} driven ependymoma cells in culture. Specifically, we observed strong inhibition of ZFTA-RELA^{fus}-driven cell growth in response to the depletion of Mertk, Ptk6, Epha1, and Acvr1 (**Fig. 2**). Among these, we extensively validated the role of Mertk in various experimental settings, including cultured mouse and patient-derived cells, tumor tissue slices, and a mouse model (**Fig. 6**). Previous studies have implicated Fgfr1 in the growth of aggressive ependymomas[16, 17]; however, the roles of the other kinases remain to be fully investigated. Notably, the inhibition of Mertk in tumors led to a significant decrease in the expression of ECM components, such as collagens and integrins (**Fig. 6, 7**). Both Acvr1, a member of the TGF-beta family, and Eph receptors are known to regulate ECM components in the tumor microenvironment[31-33]. Furthermore, recurrent ACVR1 mutations have been observed in posterior fossa ependymomas[34]. It is conceivable that the kinases identified in our screening approach could work together to regulate key biological processes in ependymoma progression. Therefore, an approach that involves targeting a combination of these kinases could be explored for more effective treatments.

Mertk, a member of the TAM family of receptor tyrosine kinases, is aberrantly expressed in several cancers, including central nervous system tumors such as astrocytoma[35] and glioblastoma[36]. Mertk signaling contributes to an immunosuppressive tumor microenvironment by inducing an anti-inflammatory cytokine profile, and modulating the functions of macrophages, myeloid-derived suppressor cells, natural killer cells, and T cells[37]. Consistently,

our data show that short-term inhibition of Mertk in tumors led to a significant decrease in the immunosuppressive cytokine Lif. Notably, Mertk inhibition also reduced *Zfta* expression, which is also a downstream target of the ZFTA-RELA^{fus}, suggesting the presence of a feed-forward loop that amplifies tumor progression (**Fig. 7C**). This feed forward loop cannot occur in the mouse model as the ZFTA-RELA fusion gene is driven by the RCAS LTR promoter rather than the ZFTA promoter as in the human case. Disrupting this loop through Mertk inhibition could completely abrogate tumor growth in human ZFTA-RELA^{fus} ependymomas. Furthermore, the substantial overlap (>80%) between genes upregulated in ZFTA-RELA^{fus} tumors and those downregulated after MRX-2843 treatment (**Fig. 7B**) supports that Mertk inhibition directly disrupts tumor-promoting pathways. Therefore, targeting Mertk in ZFTA-RELA^{fus} EPN could serve a dual purpose: directly eliminating cancer cells and transforming the microenvironment to support anti-tumor activity. Collectively, these findings highlight the therapeutic potential of targeting Mertk with MRX-2843 to suppress tumor growth and block key oncogenic pathways in ZFTA-RELA^{fus}-driven ependymomas.

In conclusion, our findings demonstrate that the ZFTA-RELA^{fus} mouse model effectively replicates human ependymoma subtype. By combining this model with a systems pharmacology-based approach, we identified Mertk as a critical kinase involved in the progression of ZFTA-RELA^{fus} -driven ependymomas. The significant impact of Mertk inhibition on tumor proliferation in preclinical models suggests that targeting this kinase could be an effective therapeutic strategy for patients with RELA fusion-driven ependymomas. These findings pave the way for further clinical evaluation of Mertk inhibitors, offering hope for improved treatments for this challenging and aggressive cancer type.

Limitations of the study. Despite the promising findings of our study, several limitations need to be addressed. Firstly, we lacked human tumor-derived models. Our studies primarily utilized patient-derived cell lines for short-term experiments, and most of our data are based on mouse ZFTA-RELA^{fus} ependymoma tumors, which is a limitation. Secondly, the mouse model of ZFTA-RELA^{fus} ependymomas is highly variable, potentially partly due to the feed forward expression loop found in humans, making it challenging to conduct long-term drug efficacy studies. Consequently, we opted to evaluate the effect of Mertk inhibition in a short-term treatment. Additionally, the rarity of these tumors means that human-derived models are scarce, presenting further challenges. Considering these limitations, our study provides a crucial foundation for the development of targeted therapies for ZFTA-RELA^{fus} -driven ependymomas and highlights the potential of Mertk inhibition as a promising therapeutic approach.

Figure Legends

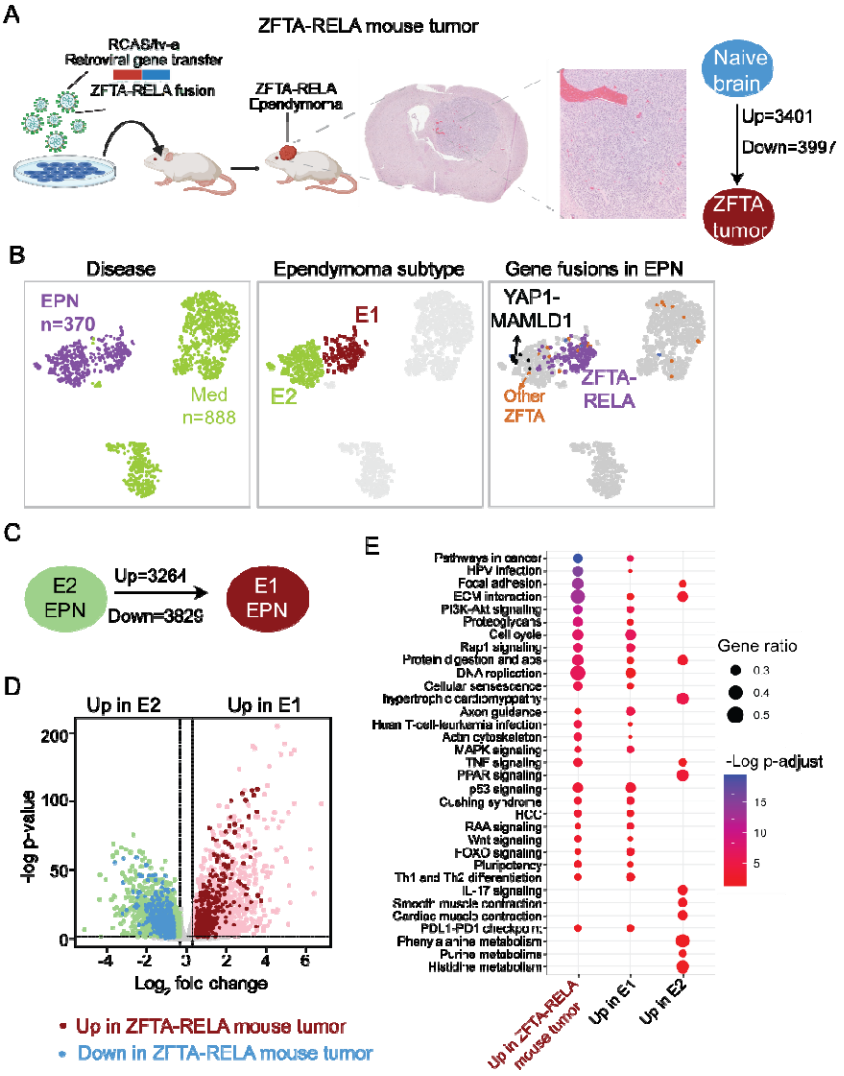

Figure 1. Subtyping human ependymomas and analyzing their comparison with the ZFTA-RELA^{FUS} mouse model. A. ***Development of the ZFTA-RELA^{fus} mouse model.*** A schematic depicting the introduction of the ZFTA-RELA^{fus} construct in DAF-1 cells, the resulting tumor development in mice, and histological sections of the mouse brain with ZFTA-RELA^{fus} tumor. Right, schematic showing number of up and down-regulated genes in ZFTA-RELA^{FUS} mouse tumor compared to naïve brain. **B.** ***Human ependymoma subtyping.*** UMAP projections showing density-based clustering analyses of human ependymoma samples (left), distinguishing subtypes E1 and E2 (middle) and gene-fusion driven markers, including ZFTA-RELA^{fus} (right). **C.** Schematic showing number of up and down-regulated genes in human E1 samples compared to human E2 ependymoma samples. **D.** Volcano plot showing the up-regulated genes (pink) and down-regulated genes (green) in E1 human samples, compared to E2 ependymoma human samples. Up-regulated and downregulated genes in ZFTA-RELA^{fus} mouse tumor compared to naïve brain are shown in red and blue respectively. **E**. Dotplot showing pathways up-regulated in ZFTA-RELA^{fus} mouse tumors compared to Naïve brain, and up-regulated pathways in E1 and E2 human ependymoma samples.

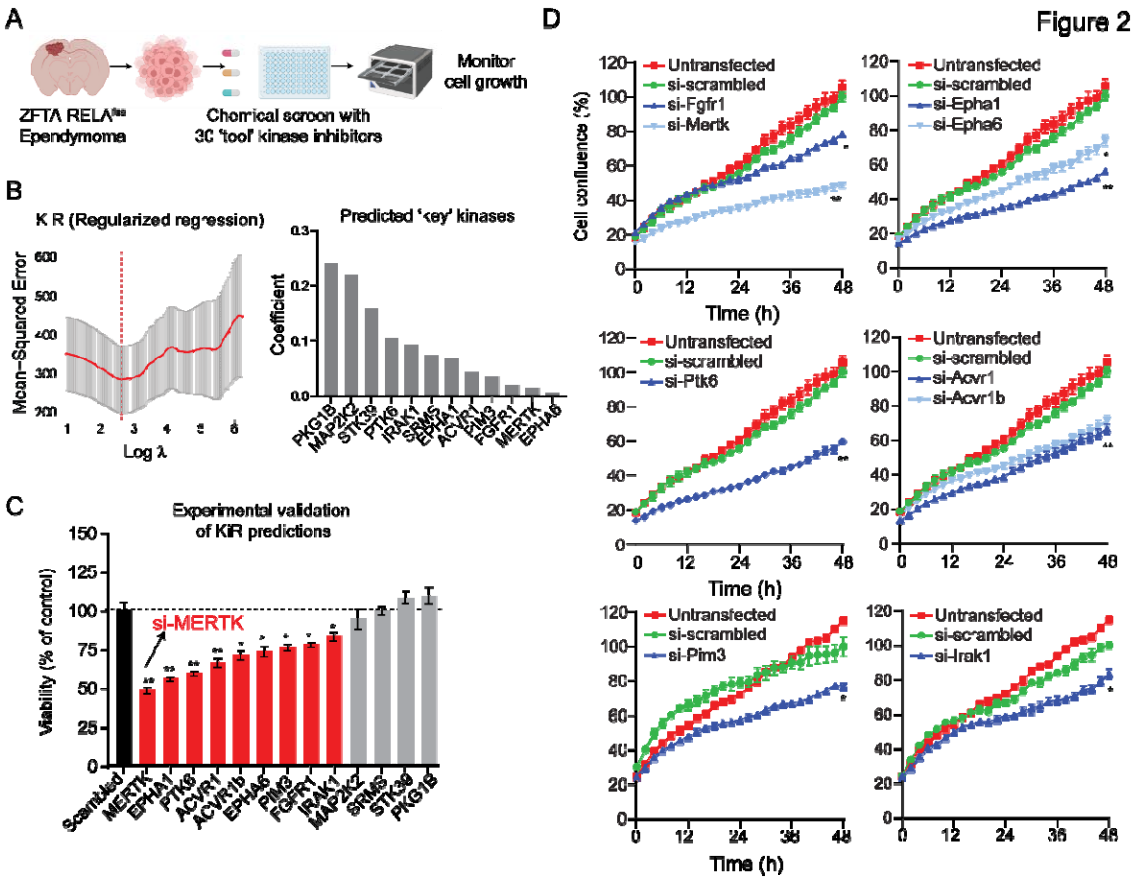

Figure 2. KiR screening identified 'key' kinases in ZFTA-RELA^{fus} ependymoma. A. A schematic of our experimental strategy for predicting kinases important for the growth of ZFTA-RELA^{fus} -expressing mouse ependymoma cells. A set of computationally chosen kinase inhibitors were evaluated for their effect on the growth of ZFTA-RELA^{fus} -expressing cells. Each compound was tested at eight different concentrations. The effect on cell growth was assessed through a real-time growth assay. **B**. KiR regularized regression plot for predicting response to kinase inhibitors in ZR1 cells. The horizontal axis represents the logarithm of the penalty hyperparameter λ, while the vertical axis shows the mean squared error from leave-one-out cross-validation (LOOCV) (mean ± SD, n = 36 folds). The dotted red line indicates the lowest error and the selected value of λ for the final model. **C.** The KiR modeling identified 12 most "informative kinases" out of over 300 kinases that influence the proliferation of ZR1. **D.** Experimental validation of KiR-predicted kinases showed that knockdown of 9 out of 12 kinases resulted in a statistically significant decrease in cell growth compared to the scrambled siRNA-transfected control. Red bars indicate the knockdown of kinases that significantly decreased cell viability. ANOVA, ** indicate $p<0.001$, * indicate $p<0.05$. **E.** Time course cell growth curves of ZFTA-RELA^{fus} ZR1 cells transfected with scrambled siRNA control or siRNAs targeting various kinases: Acvr1 and Acvr1b (top row left), Ptk6 (top row middle), Fgfr1 and Mertk (top row right), Epha1 and Epha6 (bottom row left), Irak1 (bottom row middle), and Pim3 (bottom row right). Cell confluence was assessed as the percentage of the total image area occupied by cells.

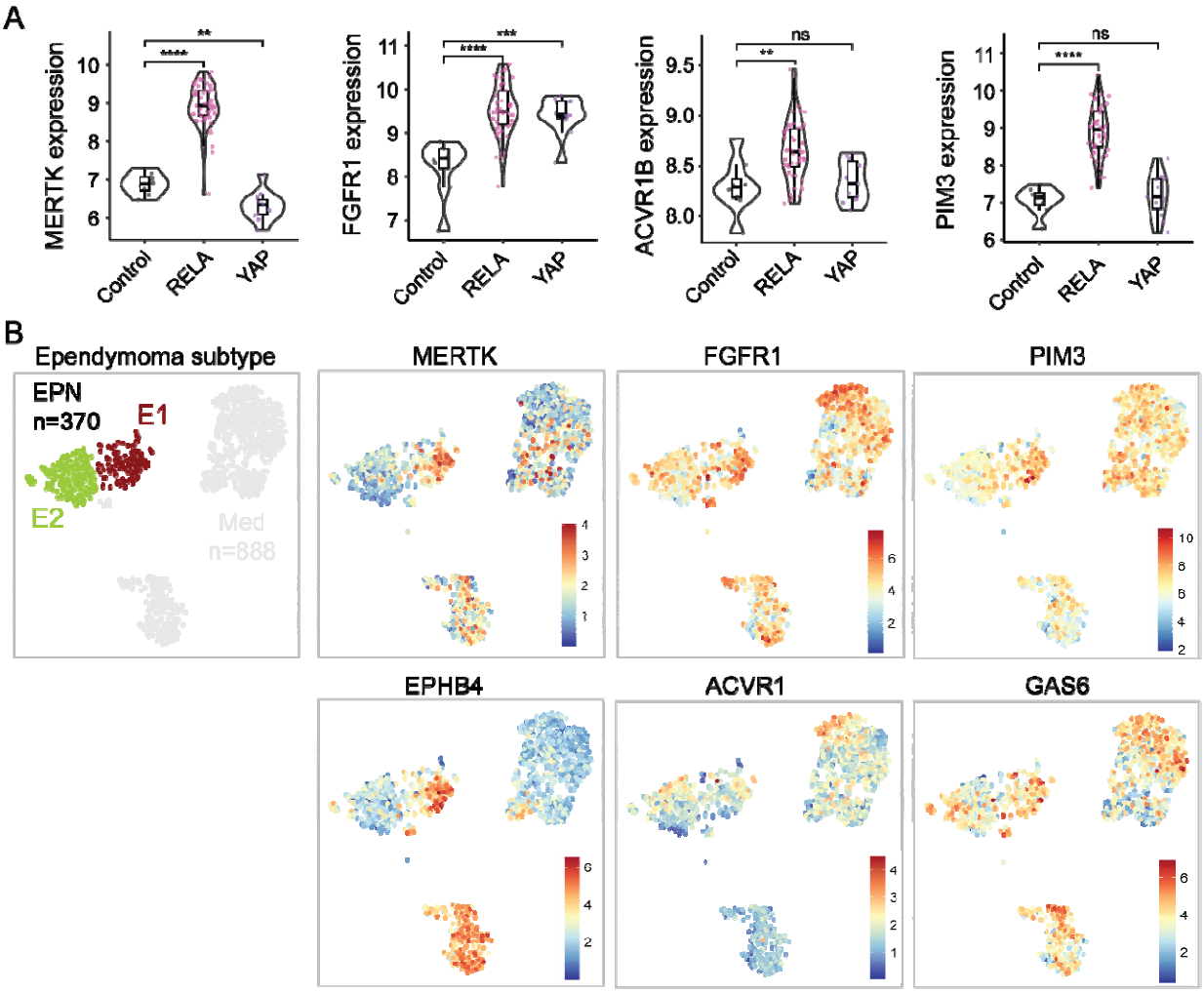

Figure 3. Elevated expression of key kinases in ZFTA-RELA^{fus} ependymomas. A. Expression of indicated kinases in human ependymoma tumors. Plots showing relative mRNA expression of *MERTK*, *FGFR1*, *ACVR1* and *PIM3* in ZFTA-RELA^{fus}, YAP^{FUS} ependymomas compared with low grade tumors from same location. Wilcox rank sum, **** indicate p<0.0001, *** indicate p<0.001. ** indicate p<0.01. **B.** UMAP projections showing density-based clustering analyses of human ependymoma samples. Clusters E1 and E2 are visualized along with the expression patterns of *MERTK*, *FGFR1*, PIM3, EPHB4, and *ACVR1B*, highlighting their enrichment in E1-specific tumor subgroups.

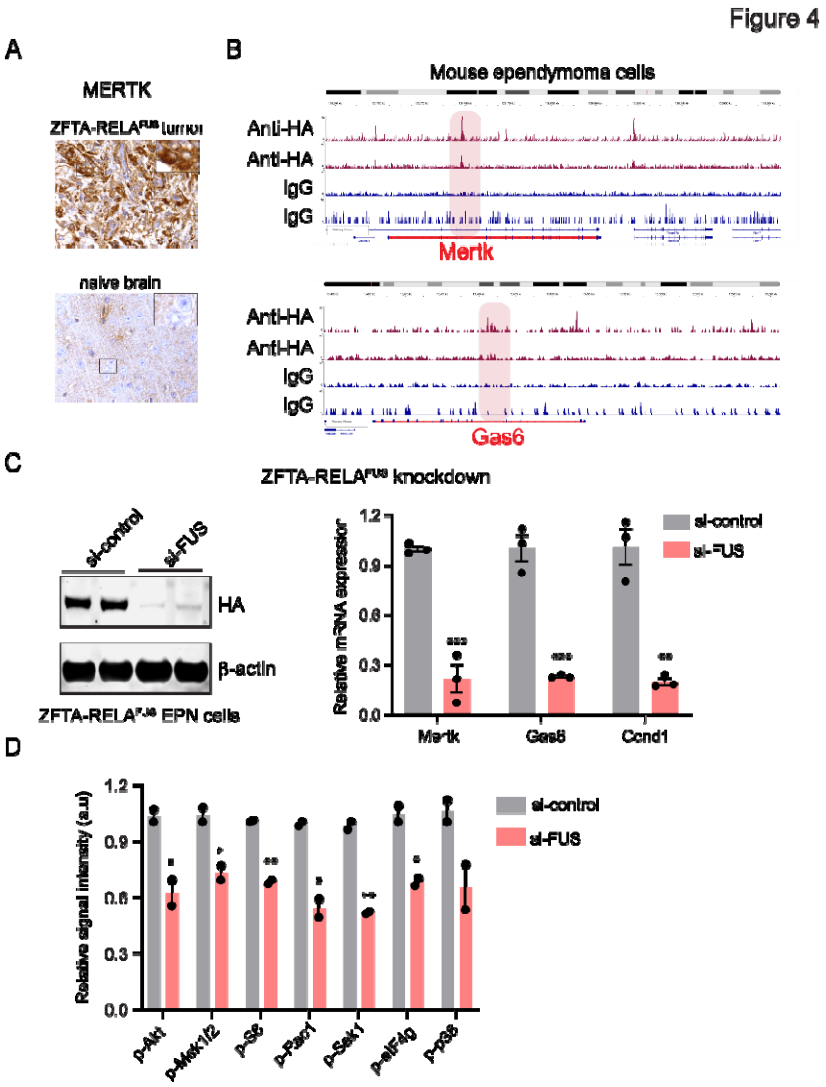

Figure 4. ZFTA-RELA^{fus} drives the expression of Mertk and Gas6. A. Representative images showing protein expression of Mertk in ZFTA-RELA^{fus} mouse tumor and naïve brain detected via immunostaining. **B**. ZFTA-RELA^{fus} binding sites were identified in the promoter regions of Mertk and Gas6 in mouse EPN cells. Anti-HA was used to pull down the ZFTA-RELA^{fus}, while IgG was used as a negative control. **C.** Knockdown of ZFTA-RELA^{fus} caused downregulation of Mertk, Gas6, and cyclin D1 (Ccnd1). *Left*, a Western blot showing the effect of siRNAs targeting RELA on the protein expression of ZFTA-RELA^{fus}, as measured by immunoblotting with HA antibody. On the right, the effect of siRNAs targeting ZFTA-RELA^{fus} on Mertk, Gas6, and Ccnd1 was assessed using quantitative PCR, with data normalized to GAPDH expression. Bars represent the mean of three replicates samples, and error bars indicate the SEM. Unpaired, two-tailed, t-test, *** indicate $p<0.0001$, ** indicate $p<0.01$. **D**. siRNAs targeting ZFTA-RELA^{fus} inhibits the phosphorylation of several pro-growth and survival signaling proteins. Bars represent the mean of two replicates and error bares represent SEM. Unpaired, two-tailed, t-test, ** indicate $p<0.01$, * indicate $p<0.05$.

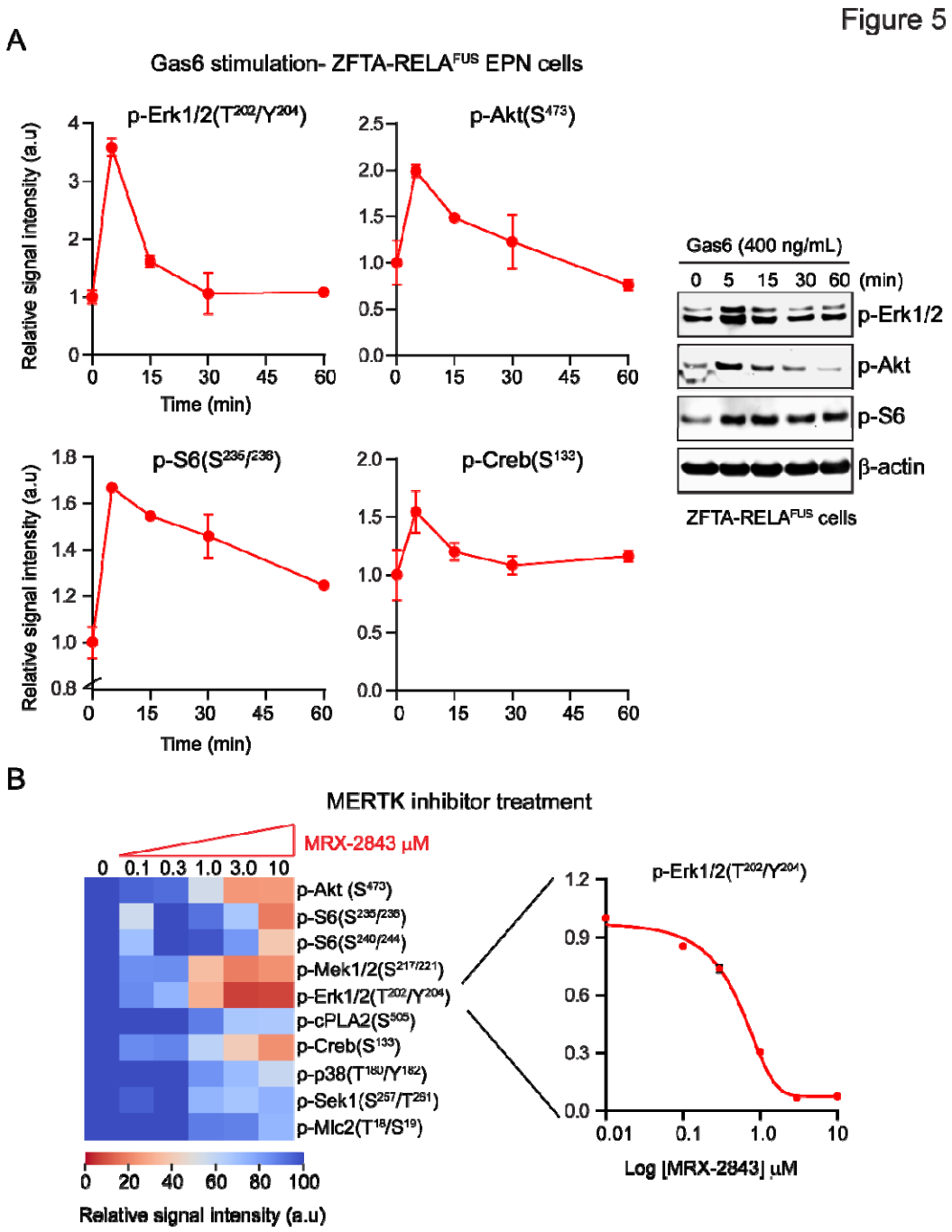

Figure 5. Gas6-Mertk signaling drives pro-growth signaling cascade in ZFTA-RELA^{fus} EPN cells. A. Gas6 stimulation caused activation of several growth factor signaling proteins in a time-dependent manner. Plots showing changes in the phosphorylation of Erk1/2, Akt (pan), S6, and Creb in ZFTA-RELA^{fus} EPN cells treated with Gas6. *Right*, representative Western blot images Phosphorylation changes were measured by Western blot. **B**. MRX2843 treatment (1 hour) inhibits several growth factors signaling proteins in a time dependent manner. A heatmap showing changes in the phosphorylation levels of Akt (pan), S6 ribosomal protein, Mek1/2, Erk1/2, cPLA2, Creb, p38, Sek1, and Mlc2 in ZFTA-RELA^{fus} EPN cells treated with the Mertk inhibitor, MRX-2843, at various concentrations (from 0.1 to 10 μM).

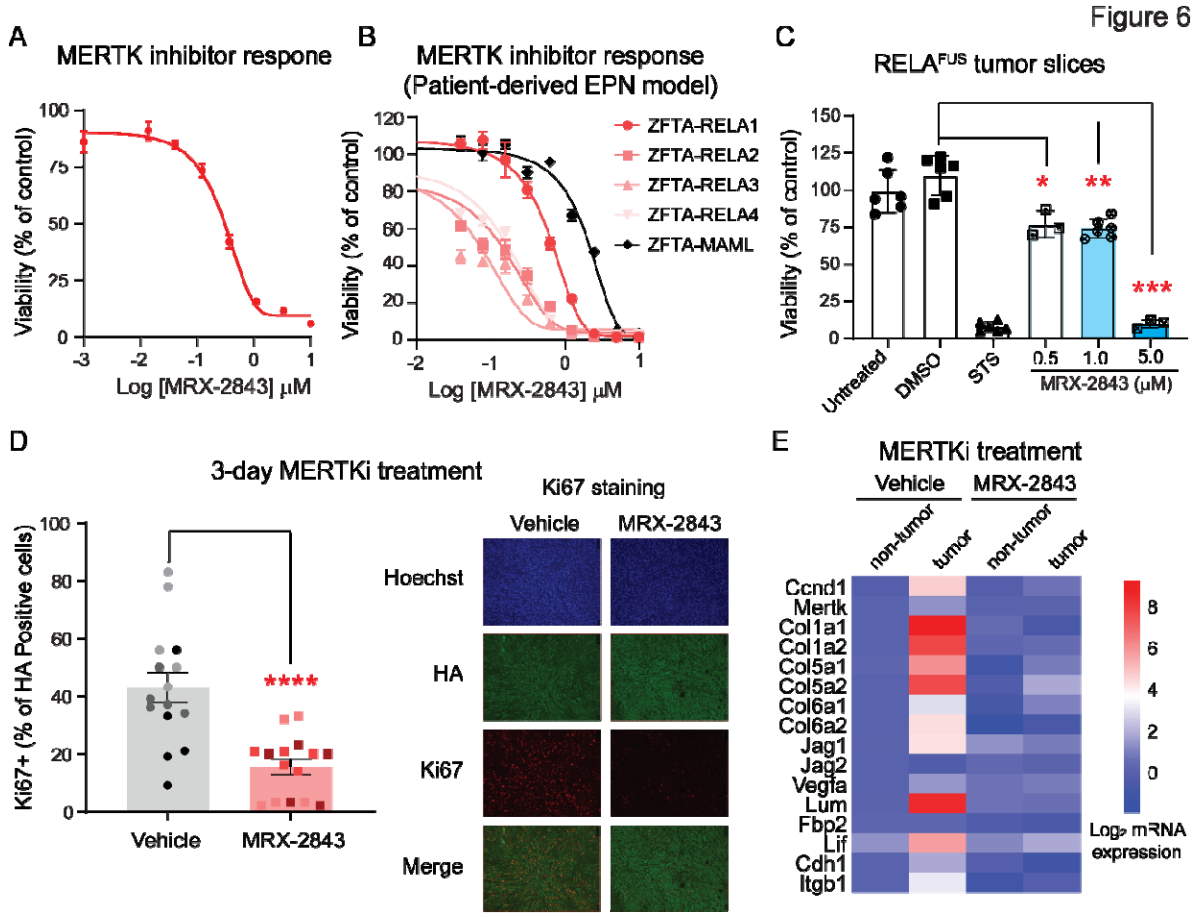

Figure 6. MERTK plays an important role in the growth of ZFTA-RELA^{fus} EPN. **A.** ZFTA-RELA^{fus} EPN cells exhibit sensitivity to MERTK inhibition by MRX-2843, showing significant effects on cell viability. **B.** Specific sensitivity of patient-derived ZFTA-RELA^{fus} EPN cells to MERTK inhibition by MRX-2843. **C.** Changes in the viability of ZFTA-RELA^{fus} patient tumor slices in response to *ex vivo* treatment with MERTK inhibitor by MRX-2843. Staurosporine (STS) was used as a positive control. * denote $p<0.05$, ** $p<0.01$, *** $p<0.001$, student's t-test. **D.** Left, A plot showing quantification of the percentage of Ki67+ cells among HA-positive cells in three tumors obtained from ZFTA-RELA^{fus} tumors treated with a control vehicle or 100 mg/kg MRX-2843 over a duration of 3 days. Right, representative immunofluorescence images showing Ki67, HA, and Hoechst staining on ZFTA-RELA^{fus} tumors, captured at 20x magnification with a scale bar of 50 μm. **E.** Heatmap showing changes in the expression of ZFTA-RELA^{fus} EPN marker genes in response to short-term MRX-2843 treatment in mice. Data are normalized vehicle-treated non-tumor tissue.

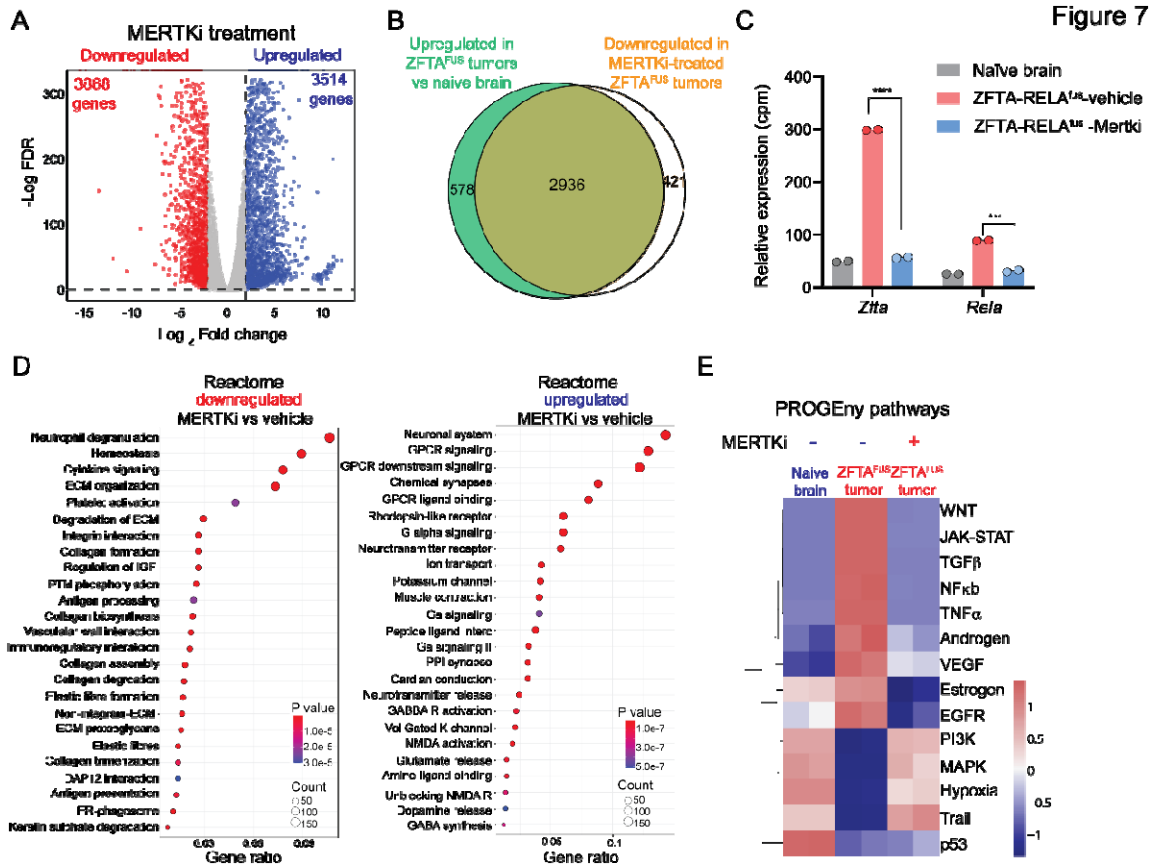

Figure 7. Mertk inhibition suppresses oncogenic pathways and alters gene expression in ZFTA-RELA^{fus} ependymomas. A. Volcano plot showing differentially expressed genes in ZFTA-RELA^{fus} tumors compared to naïve brain tissue. A total of 3,868 genes were significantly downregulated (red) and 3,514 genes were significantly upregulated (blue). **B.** Venn diagram illustrating the overlap between genes upregulated in ZFTA-RELA^{fus} tumors versus naïve brain tissue (green) and genes downregulated in Mertk inhibitor-treated ZFTA-RELA^{fus} tumors (orange). A total of 2,936 genes were commonly altered, indicating that MERTK inhibition disrupts tumor-promoting pathways. **C.** Mertk inhibition decreased the expression of both *Zfta* and *Rela* in ZFTA-RELA^{fus} tumors. **D.** GO analysis significantly downregulated (left) and upregulated (right) pathways after Mertk inhibition. Pathways are ranked based on significance (*P* value) and gene count, with colors indicating statistical significance. **E.** A heatmap depicting PROGENy pathway analysis showing significant enrichment of pro-oncogenic pathways (WNT, JAK-STAT, and NF-κB) in ZFTA-RELA^{fus} tumors, all of which are markedly downregulated after MERTK inhibition.

MATERIALS AND METHODS

Mouse modeling of ZFTA-RELA^{fus} using RCAS/tva. The RCAS/TV-A system was employed for mouse xenograft studies[38]. RCAS vector ZFTA-RELA^{fus}-HA was transfected into DF-1 cells. Neonatal mice of the Ntva, Ink4aArf, aged between 3 and 5 days, received an intercranial injection of 200,000 cells. Tumor formation was confirmed by weight loss, poor grooming leading to MRI imaging at approximately 2-3 months of age.

Mouse ZFTA-RELA^{fus} cells and reagents. The mouse ependymoma cell line ZR1 was established from ZFTA-RELA^{fus} tumors by dissociating the tumors and culturing the cells short-term. The presence of the ZFTA-RELA^{fus} fusion in the ZR1 cells was confirmed through immunofluorescence staining using an HA antibody. The cells were cultured in DMEM supplemented with 10% (v/v) fetal bovine serum (FBS), 100 IU/mL penicillin, and 100 µg/mL streptomycin. Kinase inhibitors were purchased from Selleck Chemicals (Houston, TX, USA), or Cayman Chemical Inc. (Ann Arbor, MI, USA). MRX-2843 for animal studies was obtained from MedChemExpress (Monmouth Junction, NJ, USA). Kollisolv PEG E 400, and pharmaceutical grade DMSO were purchased from Sigma-Aldrich. Normal saline was obtained from Fisher Scientific (Waltham, MA, USA). Sodium sulphobutylether-beta-cyclodextrin was acquired from AK Scientific (Union City, CA, USA).

Preparation of tissue slices. Organotypic tumor slices were prepared from mouse ependymoma tumors as described previously [39]. Fresh tumor tissues were shaped into 6 mm diameter cylinder using biopsy punches (Integra Miltex, York, PA, USA). The cores of the tumor were sliced at 250 µm thickness using a Leica VT1200 S vibrating blade microtome (Leica Biosystems, Wetzlar, Germany). The tissue cores were mounted using cyanoacrylate glue and submerged in ice-cold HBSS during slicing. The slicing parameters included a blade angle of 18°, a speed of 0.15 mm/s (with a range of 0.10 to 0.28) mm/s, and vibration amplitude of 2.0 mm. Slices were cultured on air-liquid interface using cell culture inserts in slice culture medium containing Williams' Medium supplemented with 12 mM nicotinamide, 150 nM ascorbic acid, 2.25 mg/mL sodium bicarbonate, 20 mM HEPES, 50 mg/mL glucose, 1 mM sodium pyruvate, 2 mM L-glutamine, 1% (v/v) ITS+Premix, 20 ng/mL EGF, 40 IU/mL penicillin, and 40 µg/mL streptomycin.

Viability measurements of tissue slices and drug screening. Tissue slices were incubated with Realtime-Glo MT Cell Viability reagents (Promega, Madison, WI, USA), with 50 µL medium on top. Two days from preparation, drugs were added to the tissue slices at final concentration at 0.5 µM, 1.0 µM or 5.0 µM. The slices were incubated for at least 2 hours to overnight with agitation at 100-150 rpm on an orbital shaker in a cell incubator, followed by a static incubation. Bioluminescence from tissue slices was measured using a BioTek Syngery H4 Hybrid microplate reader (BioTek, Winooski, VT, USA). Viability was calculated by the ratio of the signal at day 5 to the signals from the same tissue before treatment, then normalized to the value of vehicle control slices to be 100%.

Kinetic in vitro cell growth assay. ZR1 cells or its variants with siRNA transfection were seeded at 5,000 cells in 96-well plates. The confluence of the cells to the imaged area was evaluated using IncuCyte Live-Cell Imaging System and accompanying cell analyzer software (Essen BioScience, Ann Arbor, Michigan, USA). The inhibitor effect was normalized to the control when the control wells reached 70% confluence. To evaluate the effect of Mertk inhibitor, MRX-2843, 5,000 cells were seeded in 96-well plates, and cell viability was measured at 72-96 hours using CellTiter-Glo 2.0 reagents (Promega, Madison, WI) following the manufacturer's instructions.

Small interfering RNA transfection. All small interfering RNAs (siRNAs) were obtained from Dharmacon (Lafayette, CO, USA). siRNA's transfections in 6-well plates for expression profiling and in 96-well plates for monitoring changes in cell growth were carried out using Lipofectamine RNAiMax (Invitrogen, Waltham, MA, USA) according to the manufacturer instructions.

RNA extraction and quantitative PCR. Total cellular RNA was isolated using a GenCatch Total RNA Mini Prep Kit (Epoch Life Science, Missouri City, TX, USA). mRNA expression changes were determined using quantitative real-time PCR (qPCR). Briefly, 1 μg of total RNA was reverse transcribed into first-strand cDNA using an RT2 First Strand Kit (Qiagen, Hilden, Germany). The resultant cDNA was subjected to qPCR using gene-specific primers (BioRad, Hercules, CA, USA) and GAPDH (housekeeping control). The qPCR reaction was performed using a BioRad CFX384 thermocycler with an initial denaturation step of 10 min at 95 °C, followed by 40 cycles of 15 s at 95 °C and 60 s at 58 °C. The mRNA levels of genes encoding cytokine expression were normalized relative to the mean levels of the housekeeping gene and compared using the $2^{-\Delta\Delta Ct}$ method as described previously [40].

Western blotting. Monolayer cells were washed twice with PBS and suspended in 2% SDS lysis buffer. The remaining debris were removed by centrifuge filtration. Protein concentration was measured using a Pierce BCA protein assay kit (Thermo Scientific, #23225) with bovine serum albumin as a standard. After denaturation at 95□ for 5 min in reduced condition, 10-20 μg of proteins per lane were separated with 4-12% Bis-Tris gradient gels in MES SDS running buffer using the XCell SureLock Mini-Cell Electrophoresis System. The proteins were transferred to nitrocellulose membrane by a BioRad wet/tank blotting system. The membrane was then blocked with Licor Intercept (PBS) blocking buffer (LICOR, #927-70001) for 1 hour at ambient temperature, followed by primary antibody at 1:1000 in the blocking buffer at 4□ for overnight. Primary antibodies used were as follow: β-actin (Sigma, A1978), HA-tag (Cell Signaling Technology, CST#3724), phospho-Akt (Cell Signaling Technology, CST#4058), phospho-p44/42 MAPK (Erk 1/2) (Cell Signaling Technology, CST#4376), phospho-S6 Ribosomal protein (Cell Signaling Technology, CST#2211), and phospho-CREB (Cell Signaling Technology, CST#9198). Following PBS washes, the membrane was incubated with IRDye 800CW goat anti-Mouse IgG secondary antibody (LICOR # 926-32210) or IRDye 680RD goat anti-Rabbit IgG secondary antibody (LICOR #926-68071) at 1:5000 for 1 h at room temperature.

Signal detection was performed using the Odyssey imaging system, and the band intensities were quantified with the Odyssey imaging analysis software. Signal intensities of each protein band were normalized to that of β-actin.

Reverse-phase protein array. Molecular measurements using Reverse-phase protein arrays (RPPA) were carried out as described previously [41, 42]. Briefly, mouse ependymoma ZR1 cells treated with various concentration of MRX-2843 were washed twice in PBS, and cell lysates were prepared in 2% SDS lysis buffer as described previously [42]. Whole cell lysates were printed onto 16-pad nitrocellulose coated slides (Grace Biolabs, GBL505116) using an Aushon 2470 microarrayer (Aushon BioSystems), with each sample printed in triplicate and slides were stored at -20°C until processing. For in vivo samples, ependymoma tumors were surgically extracted from mice brain and cryopreserved until use. Small pieces of the tumors were homogenized and lysed in 2% SDS lysis buffer using a bead ruptor 12 homogenizer (Omni International 19-050A). These samples were processed similarly as to the cell lysate. The tumor lysates were adjusted to 2 mg/mL protein concentration and printed onto nitrocellulose pads attached to slide glass, with 2 depositions with single spot/sample. RPPA slides were washed with 1 M Tris-HCl (pH 9.0) for 2–4 days to remove excessive SDS residue, followed by three washes with PBS for 10 min each. Subsequently, the slides were blocked with Licor Intercept (PBS) blocking buffer for one hour at room temperature. After blocking, arrays were incubated with primary antibodies overnight at 4°C. The next day, arrays were washed thrice with PBS and then incubated with IRDye labeled secondary antibodies in the blocking buffer for 1 hour at room temperature. Following incubation, slides were scanned using a Licor Odyssey CLX Scanner (LICOR). Total signal intensity from each spot was quantified using Array-Pro analyzer software package (Media Cybernetics). The measurement of a specific protein from an individual sample was normalized to its total β-actin (Sigma, A1978).

Drug treatment of EPN bearing mice. Mice with confirmed tumors by MRI were randomly assigned to receive either a vehicle or 50 mg/kg of MRX-2843. Treatment was administered once daily via oral gavage for either 3 or 5 consecutive days. Mice were euthanized one hour after the final treatment, and the whole brains were harvested for further analysis.

RNASeq sequencing and analysis. Total RNA was extracted from naïve brain tissue and ZFTA-RELA^{fus} rumors using the RNeasy Mini Kit (QIAGEN). RNA was quantified and assessed for quality using a Nanodrop spectrophotometer (Thermo Fisher). Library prep and RNA sequencing was performed and analyzed at Novogene using a standing workflow with sample quality control (assessed through Library QC) and polyA enrichment. Sequencing was then performed using 150 bp paired-end reads on the Illumina PE150 platform. Raw counts for samples were obtained by aligning sequencing reads to the mm10_assembly reference genome using the STAR aligner (v2.7.7a)[43]. The aligned files were then indexed with SAMtools (v1.19.2), and gene expression levels were quantified using featureCounts. All raw counts were normalized using log transformed TPM (Transcripts Per Million) values. Differential gene expression analysis was performed between ZFTA-RELA^{fus} vs Naïve brain mouse tumors,

using the R/Bioconductor package DESeq2[44] (v 1.44.0and a statistical cutoff of FDR < 0.05 and FC > 1.5 was applied to obtain differentially regulated genes. Raw data files have been deposited to the NCBI Gene Expression Omnibus under accession number GEO: GSE000000. GO and Reactome Pathway enrichment analysis was done using R Bioconductor Packages enrichR[45] (v 3.2) and dot plots were made using R Bioconductor package ggplot2. Heatmaps were made using R package pheatmap[46] (v 1.0.12). For human ependymoma samples, UMAP coordinated were obtained from Arora *et al*[5] and replotted to make figures in 1. The differential expression results were obtained from Supplemental Table from Arora et al and used to make volcano plots.

Immunohistochemistry. Harvested brain samples were fixed in 10% buffered formalin phosphate for 48 hours, followed by coronal slicing and processing into paraffin-mounted blocks. Sections of 5 μm thickness were cut and mounted onto charged slides for staining. Hematoxylin and eosin (H&E) staining were performed for tumor verification. Subsequently, DAB antibody staining using a Ventana system was conducted. Stains targeting HA and Ki67 were applied to evaluate proliferation effects on tumor cells with MRX-2843 treatment.

Immunofluorescence. Immunofluorescent (IF) staining was performed to co-localize HA and Ki67 using Alexa 488 and Cy3, respectively, while Hoechst stain was used for visualizing cell nuclei. This enabled the assessment of the percentage of ZFTA-RELA^{fus} positive cells also positive for Ki67. QuPath software was utilized for IF stain analysis. Each tumor was divided into five 0.5 mm x 0.6 mm sections at 20x magnification, covering the majority of the tumor. Positive counts for ZFTA-RELA^{fus} positive cells were organized into positive and negative counts based on co-staining for Ki67. Minimum intensity thresholds were applied before overlaying ZFTA-RELA^{fus} positive cells with Ki67 positive cells to ensure accurate identification of all positive cells. Positive counts in each section were then expressed as a percentage of all ZFTA-RELA^{fus} positive cells and compared across treatment groups.

REFERENCES

1. Ruda, R., Gilbert, M. & Soffietti, R. Ependymomas of the adult: molecular biology and treatment. *Current opinion in neurology* **21**, 754-761 (2008).
2. Pajtler, K.W. et al. The current consensus on the clinical management of intracranial ependymoma and its distinct molecular variants. *Acta neuropathologica* **133**, 5-12 (2017).
3. Pajtler, K.W. et al. Molecular classification of ependymal tumors across all CNS compartments, histopathological grades, and age groups. *Cancer cell* **27**, 728-743 (2015).
4. Parker, M. et al. C11orf95–RELA fusions drive oncogenic NF-κB signalling in ependymoma. *Nature* **506**, 451-455 (2014).
5. Arora, S. et al. Transcriptomic landscape identifies two unrecognized ependymoma subtypes and novel pathways in medulloblastoma. *bioRxiv*, 2024.2010. 2021.619495 (2024).
6. Gujral, T.S., Peshkin, L. & Kirschner, M.W. Exploiting polypharmacology for drug target deconvolution. *Proc Natl Acad Sci U S A* **111**, 5048-5053 (2014).
7. Bello, T. et al. Computational modeling identifies multitargeted kinase inhibitors as effective therapies for metastatic, castration-resistant prostate cancer. *Proceedings of the National Academy of Sciences* **118**, e2103623118 (2021).
8. Gujral, T.S. et al. A noncanonical Frizzled2 pathway regulates epithelial-mesenchymal transition and metastasis. *Cell* **159**, 844-856 (2014).
9. Bello, T. et al. KiRNet: Kinase-centered network propagation of pharmacological screen results. *Cell Rep Methods* **1** (2021).
10. Chan, M. et al. Machine learning identifies molecular regulators and therapeutics for targeting SARS□CoV2□induced cytokine release. *Molecular systems biology* **17**, e10426 (2021).
11. Arang, N. et al. Identifying host regulators and inhibitors of liver stage malaria infection using kinase activity profiles. *Nat Commun* **8**, 1232 (2017).
12. Olson, A.T. et al. Polypharmacology-based kinome screen identifies new regulators of KSHV reactivation. *Plos Pathogens* **19**, e1011169 (2023).
13. Chan, M., Kang, Y., Osborne, S., Zager, M. & Gujral, T. KinCytE-a Kinase to Cytokine Explorer to Identify Molecular Regulators and Potential Therapeutic Opportunities. *bioRxiv*, 2023.2008. 2020.554063 (2023).
14. Ozawa, T. et al. A de novo mouse model of C11orf95-RELA fusion-driven ependymoma identifies driver functions in addition to NF-κB. *Cell reports* **23**, 3787-3797 (2018).
15. Ozawa, T. et al. C11orf95-RELA fusion drives aberrant gene expression through the unique epigenetic regulation for ependymoma formation. *Acta Neuropathologica Communications* **9**, 1-21 (2021).

16. Lehtinen, B. et al. Clinical association analysis of ependymomas and pilocytic astrocytomas reveals elevated FGFR3 and FGFR1 expression in aggressive ependymomas. *BMC cancer* **17**, 1-12 (2017).
17. Lötsch, D. et al. Targeting fibroblast growth factor receptors to combat aggressive ependymoma. *Acta neuropathologica* **142**, 339-360 (2021).
18. Liu, G., Park, Y.-J. & Abraham, E. Interleukin□1 receptor□associated kinase (IRAK)□1□mediated NF□κ activation requires cytosolic and nuclear activity. *The FASEB Journal* **22**, 2285-2296 (2008).
19. Arabzade, A. et al. ZFTA-RELA dictates oncogenic transcriptional programs to drive aggressive supratentorial ependymoma. *Cancer discovery* (2021).
20. Kupp, R. et al. ZFTA-translocations constitute ependymoma chromatin remodeling and transcription factors. *Cancer discovery* (2021).
21. Tworkoski, K.A. et al. MERTK controls melanoma cell migration and survival and differentially regulates cell behavior relative to AXL. *Pigment cell & melanoma research* **26**, 527-541 (2013).
22. Cummings, C.T., DeRyckere, D., Earp, H.S. & Graham, D.K. Molecular pathways: MERTK signaling in cancer. *Clinical Cancer Research* **19**, 5275-5280 (2013).
23. Davra, V. et al. Axl and Mertk Receptors Cooperate to Promote Breast Cancer Progression by Combined Oncogenic Signaling and Evasion of Host Antitumor Immunity. *Cancer Research* **81**, 698-712 (2021).
24. Su, Y.-T. et al. MerTK inhibition decreases immune suppressive glioblastoma-associated macrophages and neoangiogenesis in glioblastoma microenvironment. *Neuro-oncology advances* **2**, vdaa065 (2020).
25. Wu, J. et al. MerTK as a therapeutic target in glioblastoma. *Neuro-oncology* **20**, 92-102 (2018).
26. Liang, M.-L. et al. Significance of cyclin D1 overexpression in progression and radio-resistance of pediatric ependymomas. *Oncotarget* **9**, 2527 (2017).
27. Hallett, R.M. et al. Therapeutic targeting of LIF overcomes macrophage-mediated immunosuppression of the local tumor microenvironment. *Clinical Cancer Research* **29**, 791-804 (2023).
28. Schubert, M. et al. Perturbation-response genes reveal signaling footprints in cancer gene expression. *Nature communications* **9**, 20 (2018).
29. Wong, S. & Witte, O.N. The BCR-ABL story: bench to bedside and back. *Annu. Rev. Immunol.* **22**, 247-306 (2004).
30. Roskoski Jr, R. Properties of FDA-approved small molecule protein kinase inhibitors: A 2024 update. *Pharmacological research*, 107059 (2024).
31. Nagar, G. et al. Multi-omics therapeutic perspective on ACVR1 gene: from genetic alterations to potential targeting. *Briefings in Functional Genomics* **22**, 123-142 (2023).
32. Fattet, L. et al. Matrix rigidity controls epithelial-mesenchymal plasticity and tumor metastasis via a mechanoresponsive EPHA2/LYN complex. *Developmental cell* **54**, 302-316. e307 (2020).
33. Wu, Y. et al. The functions of EphA1 receptor tyrosine kinase in several tumors. *Current Medicinal Chemistry* **30**, 2340-2353 (2023).
34. Pratt, D. et al. Recurrent ACVR1 mutations in posterior fossa ependymoma. *Acta neuropathologica* **144**, 373-376 (2022).

35. Keating, A.K. et al. Inhibition of Mer and Axl receptor tyrosine kinases in astrocytoma cells leads to increased apoptosis and improved chemosensitivity. *Molecular cancer therapeutics* **9**, 1298-1307 (2010).
36. Wang, Y. et al. Mer receptor tyrosine kinase promotes invasion and survival in glioblastoma multiforme. *Oncogene* **32**, 872-882 (2013).
37. Huelse, J.M., Fridlyand, D.M., Earp, S., DeRyckere, D. & Graham, D.K. MERTK in cancer therapy: Targeting the receptor tyrosine kinase in tumor cells and the immune system. *Pharmacology & therapeutics* **213**, 107577 (2020).
38. Kanvinde, P.P. et al. Leveraging the replication-competent avian-like sarcoma virus/tumor virus receptor-A system for modeling human gliomas. *Glia* **69**, 2059-2076 (2021).
39. Sivakumar, R. et al. Organotypic tumor slice cultures provide a versatile platform for immuno-oncology and drug discovery. *Oncoimmunology* **8**, e1670019 (2019).
40. Gujral, T.S. & MacBeath, G. A system-wide investigation of the dynamics of Wnt signaling reveals novel phases of transcriptional regulation. *PLoS One* **5**, e10024 (2010).
41. Gujral, T.S. et al. Profiling phospho-signaling networks in breast cancer using reverse-phase protein arrays. *Oncogene* **32**, 3470-3476 (2013).
42. Gujral, T.S. & Kirschner, M.W. Hippo pathway mediates resistance to cytotoxic drugs. *Proc Natl Acad Sci U S A* **114**, E3729-E3738 (2017).
43. Dobin, A. et al. STAR: ultrafast universal RNA-seq aligner. *Bioinformatics* **29**, 15-21 (2013).
44. Love, M.I., Huber, W. & Anders, S. Moderated estimation of fold change and dispersion for RNA-seq data with DESeq2. *Genome Biol* **15**, 550 (2014).
45. Chen, E.Y. et al. Enrichr: interactive and collaborative HTML5 gene list enrichment analysis tool. *BMC Bioinformatics* **14**, 128 (2013).
46. Kolde, R. (2018).